High-performance large-area perovskite photovoltaic modules

Liang Chu[1] (✉), Shuaibo Zhai[2], Waqar Ahmad[3], Jing Zhang[4] (✉), Yue Zang[1], Wensheng Yan[1] (✉), and Yongfang Li[5]

[1] Institute of Carbon Neutrality and New Energy & School of Electronics and Information, Hangzhou Dianzi University, Hangzhou 310018, China
[2] School of Electronic and Optic Engineering, Nanjing University of Posts and Telecommunications, Nanjing 210023, China
[3] Department of Physics, Faculty of Sciences, University of Sialkot, Punjab 51310, Pakistan
[4] School of Materials Science & Engineering, Jiangsu Collaborative Innovation Center of Photovoltaic Science & Engineering, Changzhou University, Changzhou 213164, China
[5] Beijing National Laboratory for Molecular Sciences, CAS Key Laboratory of Organic Solids, Institute of Chemistry, Chinese Academy of Sciences, Beijing 100190, China

ABSTRACT

Perovskite solar cells (Pero-SCs) exhibited a bright future for the next generation of photovoltaic technology because of their high power conversion efficiency (PCE), low cost, and simple solution process. The certified laboratory-scale PCE has reached 25.7% referred to small scale (< 0.1 cm^2) of Pero-SCs. However, with the increase of the area to module scale, the PCE drops dramatically mainly due to the inadequate regulation of growing large-area perovskite films. Therefore, there is a dire need to produce high-quality perovskite films for large-area photovoltaic modules. Herein, we summarize the recent advances in perovskite photovoltaic modules (PPMs) with particular attention paid to the coating methods, as well as the growth regulation of the high-quality and large-area perovskite films. Furthermore, this study encompasses future development directions and prospects for PPMs.

KEYWORDS

perovskite solar cells, perovskite films, large area, perovskite photovoltaic modules

1 Introduction

At present, perovskite solar cells (Pero-SCs) have attracted great attention from both academia and industry due to their unique advantages [1, 2]. Its suitable optoelectronic properties for photovoltaic applications such as flexible direct bandgap, broad absorption spectra, long carrier diffusion length, and high carrier mobility [3–6] led to the rapid development of Pero-SCs reaching the record power conversion efficiency (PCE) of certified 25.7%. In particular, the high-efficiency Pero-SCs can be manufactured through a low-cost solution process, which shows charming prospects for future commercialization. Despite these enormous achievements, Pero-SCs with high efficiency are usually fabricated with an area of less than 0.1 cm^2. However, enlarging the perovskite films for efficient and stable photovoltaic modules remains difficult for commercialization [7, 8].

For industrial applications, the photovoltaic modules are categorized as large module (> 14,000 cm^2), standard module (6,500–14,000 cm^2), small module (800–6,500 cm^2), and mini-module (200–800 cm^2). According to National Renewable Energy Laboratory (NREL) "champion photovoltaic module efficiency chat", the first certified PCE (11.7%) of perovskite photovoltaic modules (PPMs) was reported by Toshiba in 2018 for mini-module of 703 cm^2 [9]. In 2019, Microauanta successively achieved 11.98% and 14.24% certified PCE for mini-modules. In 2020, Panasonic delivered the certified PCE of 16.1% for an 802 cm^2 PPM. Later, Panasonic refreshed the certified PCE of 17.9% on a PPM with 804 cm^2 area. Recently, Utmolight reported 18.2% record PCE for 300 cm^2 modules. In comparison with the above module, the laboratory PPMs are usually less than 100 cm^2, and the highest PCE is about 21% [10, 11]. From the above efficiency evolution, it is found that the certified PCE of large-area PPMs is far behind that of small-area Pero-SCs, which is mainly ascribed to the four aspects: (1) non-uniform large-area deposition of perovskite films and other function layers, (2) increment of series resistance and decrement of parallel resistance in PPMs, (3) dead area for connecting independent sub-cell units, and (4) local perovskite degradation at the etched edges of P2 lines.

For manufacturing large-area PPMs towards industrialization, lots of issues are needed to be solved, such as relatively low efficiency of large-area PPMs, preparation of large-area and high-quality perovskite films, and design of interconnected

sub-cells to composite modules. The prerequisite is to deposit large-area perovskite films with high uniformity and reproducibility. The architecture prototype of Pero-SCs is a sandwich structure usually including electron transport layer (n), perovskite film, hole transport layer (p), and top electrode. The top electrodes are metal or carbon conductive materials, which can be easily deposited for large area by respective thermal evaporation or printing methods [12, 13]. The electron and hole transport layers can also be easily formed by industrial large-area technologies. However, it is difficult to expand the perovskite films with high quality from small-area to large-area modules [14]. Nowadays, the schemes of depositing large-area perovskite films are still varied, without a standardized industrial scale. Importantly, the thickness, crystallinity, surface roughness and compactness of perovskite films directly affect their absorption, charge generation and separation, and device performance [15–17].

In this review, we divide the following study into three main sections: Firstly, we introduce the fundamentals of nucleation and crystallization for solution-process perovskite films to understand the next coating methods, and the solvent engineering to control the crystallization kinetics of the perovskite films; secondly, we analyze the various coating methods films, identify their main limitations, and provide insights for large-area perovskite films; lastly, we present the development directions of PPMs for future commercial applications.

2 Forming mechanism of perovskite films

The low-cost solution process is one of the most factors to introduce the future commercialization of perovskite photovoltaic technology. The LaMer model explains the nucleation and growth mechanism in perovskite films (Figs. 1(a) and 1(b)), which contains three different stages: (i) pre-nucleation, (ii) burst-nucleation, and (iii) growth [18–22]. With evaporating solvent continuously, the solution concentration increases, and the nuclei generate. Meanwhile, the continuous consumption of solute with nucleation and growth leads to the effect of decreasing the solution concentration. After coating the wet films with subsequent heating, the solution gradually evaporates and the concentration attains supersaturation (C_c) (stage I). In stage II, perovskite nuclei start to form and grow while the solution attains a critical concentration of C_c to overcome the energy barrier for nucleation. When the solute consumption is faster than the solvent evaporation, the solution concentration drops below C_c, and there is only growth existence of the formed nuclei without forming new nuclei (stage III). Thus, the quality of perovskite films can be tuned by either nucleation or growth control.

Based on the thermodynamic homogeneous nucleation [19, 23], continuous evaporation of solution in wet films leads to perovskite nuclei formation and the perovskite nucleus grows gradually up to the critical nucleation radius of rc, as shown in Fig. 1(c). The nucleation rate can be described by the critical Gibbs free energy of ΔG_c, which needs to be overcome as a barrier to achieving the transition from I to II stage in Figs. 1(a) and 1(b). The transition is also a process from solution state to nucleation and growth. Significantly, once the perovskite nucleation begins, the process will happen very rapidly and is difficult to control. Thus, the supersaturation (C_s) is relatively easier to be controlled for nucleation to regulate the perovskite films. To date, solvent engineering has been frequently used to
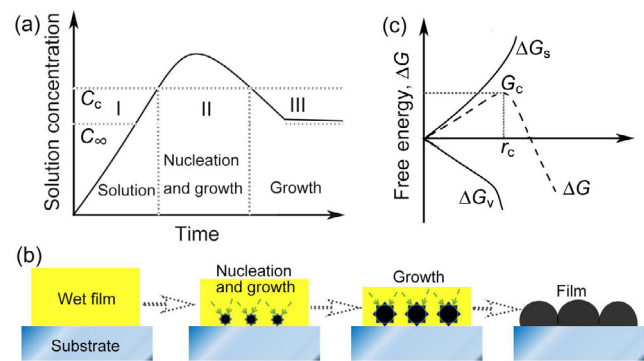
Figure 1 (a) LaMer schematic diagram for the nucleation and growth of perovskite films, where C_∞ and C_c are the equilibrium concentration of solute with the bulk solid and the critical minimum concentration for nucleation, respectively. (b) Corresponding schematic illustration for nucleation and growth of perovskite films at each stage. (c) Free energy diagram for nucleation. ΔG_s: surface free energy, ΔG_v: bulk free energy, ΔG: total free energy, ΔG_c: critical free energy, and r_c: critical radius of nucleus.

control the natural nucleation for high-quality perovskite films, such as anti-solvent [24], pumping vacuum [25], gas-quenching [26], and additive engineering [27], which can promote the nucleation speed, and prolong precursor-processing window and short-grain growth rate to favor the preparation of high-quality perovskite films with large gains.

3 Coating methods

To date, a series of coating methods have been applied to deposit large-area perovskite films, including doctor blade, slot-die, spray, ink-jet, screen printing, soft-cover deposition, vacuum deposition, as well as spin coating. Meanwhile, various strategies have been adopted to control the nucleation and growth of the perovskite films. The coating methods of other charge transporting layers are accompanied by the introduction of perovskite films. Next, we briefly summarize the coating methods for large-area PPMs.

3.1 Spin coating

Spin coating is the simplest synthesis method used in laboratory for deposition of small-area Pero-SCs. In general, spin coating is a solution-based synthesis method whereby the precursor solution is dropped on the substrates and then rotated at a high speed to form thin films during the spin process. This method can be divided into "one-step" and "two-step" processes. For the one-step spin-coating method, the perovskite precursor in one solution is rotated to form perovskite films. In the two-step method, the PbX$_2$ (X = I, Br, Cl) solution is firstly spin-coated for films, which then turn to the perovskite films in the next step [29]. However, the precursor solution is wasted seriously in the spin-coating process. Notably, the spin coating method cannot suit to form larger-area uniform perovskite films. As for the relatively small-area modules (less than 10 cm × 10 cm), there are also previous reports of the spin-coating method to prepare PPMs [11, 30–32]. To the best of our knowledge, the maximum area of the effective spin-coated PPMs is 10 cm × 10 cm, where the PCE approached 18.0% [30].

Solvent engineering can control the nucleation and growth of large-area perovskite films for improving the performance of PPMs. Till now, the antisolvent quenching is still the most

used strategy to form uniform perovskite films. Figure 2(a) shows the typical spin coating of large-area PPMs using the architecture of "FTO/SnO$_2$/perovskite/Spiro-OMeTAD/Au" (FTO = fluorine-doped tin oxide) [30]. The P1, P2, and P3 were etched by a laser to form the module substrate with 12 strips. The SnO$_2$ electron transport layer was deposited by chemical bath deposition, and the perovskite film, as well as spiro-OMeTAD hole transport layer, were all fabricated by the spin-coating method. The antisolvent dropping at the center of the spinning film cannot interact with the whole 10 cm × 10 cm wet film, leading to the inhomogeneous perovskite film (Fig. 2(b)). On another hand, the antisolvent moving from the center to the edge of substrate during dropping can extract the solvent of the whole wet film to form a homogenous large-area perovskite film (Fig. 2(c)). According to the movement of the syringe, the perovskite film shows good uniform and pinhole-free morphology.

In 2018, Jung's group introduced anisole as the antisolvent into the one-step spin-coating perovskite films with an ultrawide processing window by varying dimethylformamide (DMF):dimethyl sulfoxide (DMSO) ratio, and successfully fabricated uniform perovskite films as large as 100 cm^2 [31]. In 2019, they fabricated large-area SnO$_2$ electron transport layers by an electrostatic self-assembly method through the attraction between the negatively charged SnO$_2$ colloids and FTO substrate and then deposited perovskite films by the above spin-coating method [29]. The PCE of 100 cm^2 PPMs achieved 14.0% without shunt resistance loss. Liu et al. used spin-coating method with Cs$^+$ additive engineering to obtain a PCE of 21.08% for PPMs with an active area over 30 cm^2, which demonstrates better reproducibility and stability than the methylammonium lead iodide (MAPbI$_3$)-based modules with the PCE of 18.26% [11]. Recently, Dai's and Nazeeruddin's groups described the surface passivation of spin-coated perovskite films using ortho-(phenylene)di(ethylammonium)iodide for PPMs with an active area of 26 cm^2 led to a record efficiency of 21.4% [32].
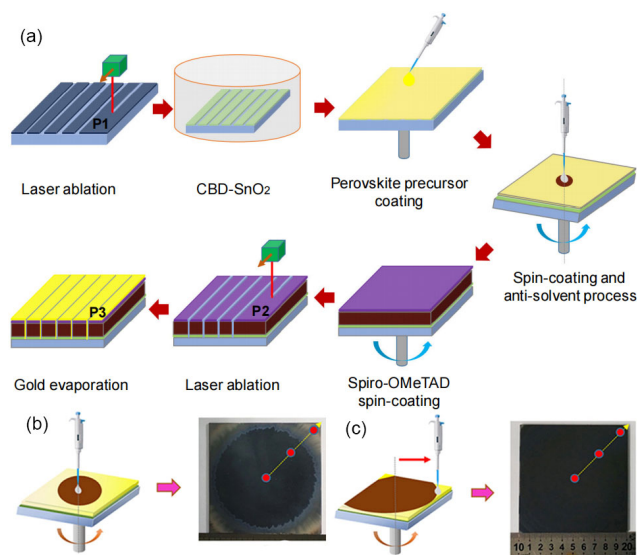

Figure 2 (a) Illustration of the procedure for PPMs fabrication. Schematic diagrams and photographs of the 10 cm × 10 cm perovskite film by (b) antisolvent quenching process on the center and (c) dynamic antisolvent quenching process from the center to the edge. Reproduced with permission from Ref. [30], © WILEY-VCH Verlag GmbH & Co. KGaA, 2019.

3.2 Doctor blading

For large-area PPMs, doctor blading is a traditional skillful technology for the substitution of spin-coating method [33]. A perovskite precursor solution is coated on the surface of substrate to form wet films through the scraper movement. The thickness of the perovskite films can be controlled by managing the precursor concentration, distance of scraper with the substrate, coating speed and blade pressure [34]. In addition, the nature of the solvent evaporation and the inherent solution flow dynamics in blade process can significantly affect the processing window to tune the perovskite film quality and device photovoltaic performance. They have been controlled, such as solvent engineering [34], substrate heating [35], and gas-assisted drying [36–39]. Compared to the spin-coating method, doctor blading has obvious advantages of raw material saving, easy equipment cleaning, simple and stable process. But the supply of perovskite precursor solution is not automated. Thus, the doctor-blading method is suitable for the small-scale production of PPMs.

In 2014, blade-coating was first introduced to deposit perovskite films for small-area Pero-SCs and showed significantly improved air stability with PCE of 9.52% [33]. In 2015, Huang's group blade-coated perovskite films with large domain and concentric ring photonics structure. The precursor solution drying in the doctor-blade coating process is responsible for the formation of the large domains and the coffee-ring-like perovskite photonic structures, whose periodicity can be well tuned by the substrate temperature and the precursor solution concentration [40]. In 2017, it was demonstrated that antisolvent treatment by formulating solvents prolonged the precursor-processing window up to 8 min and shorted the grain growth rate as 1 min in blade coating [34]. In addition, the excess methylammonium chloride (MACl) in MAPbI$_3$ precursor widened the thermal processing window to achieve a highly crystalline film. At last, a 12.6-cm^2 four-cell module achieved 13.3% stabilized efficiency. In 2018, Huang's group heated the substrate (typically 70–145 °C) to speed up the blade coating rate and suppress the formation of needle-like structures for large-area perovskite films [35]. Meanwhile, a tiny surfactant dramatically changed the solvent evaporation and increased the adhesion of the perovskite precursor solution. The surfactant at the surface reduced the surface energy and created a surfactant concentration gradient. The high concentration of surfactant in the center reduced the surface tension, generating Marangoni flow in a direction reverse to the original solute flow for equilibrium. Fast blading perovskite films in air led to stabilized module efficiencies of 15.3% and 14.6% with aperture areas of 33.0 and 57.2 cm^2, respectively. In 2019, they reported a method to accelerate the drying of wet perovskite films at room temperature by introducing an N$_2$ knife (Fig. 3(a)) [36]. A 2% volatile noncoordinating solvent (VNCS) was introduced into the nonvolatile coordinating solvent (NVCS) to dissolve the perovskite powder, which achieved rapid drying at room temperature and larger perovskite grains (Fig. 3(b)). Subsequently, they expand N$_2$-knife assisted doctor blading perovskite on flexible and textured silicon substrates for a record aperture efficiency of 15.86% on modules with an area of 42.9 cm^2 and 26%-efficient monolithic perovskite/silicon tandem solar cells, respectively [37, 38].

In 2021, Huang's group found that the DMSO at the buried layer could induce high-density voids in the N$_2$-knife assisted
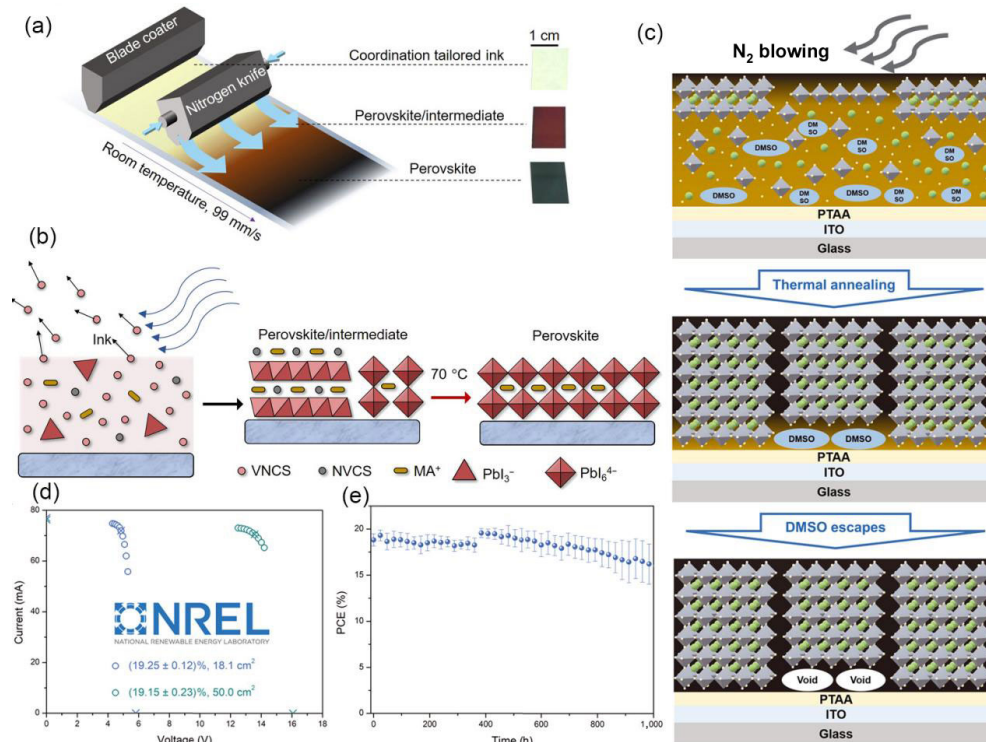
Figure 3 (a) Schematic illustration for N₂-knife-assisted blade coating of perovskite films at 99 mm/s at room temperature using coordination tailored ink. Insets: photograph images of wet, perovskite/intermediate and perovskite films. (b) Schematic illustration of the wet film drying into perovskite/intermediate film and perovskite film with full crystallization. Reproduced with permission from Ref. [36], © Deng, Y. H. et al. 2019. (c) Schematic illustration for the void formation at the buried interfaces, (d) NREL certified performance of PPMs with aperture areas of 18.1 and 50.0 cm². (e) Long-term operational stability of five PPMs under simulated 1-sun illumination at 50 °C. Reproduced with permission from Ref. [39], © Chen, S. S. et al. 2021.

doctor blading process, which will accelerate film degradation under illumination [39]. They partially replaced DMSO with solid carbohydrazide coordination additive to reduce the formation of interface voids (Fig. 3(c)). The blade-coated p-i-n PPMs with aperture areas of 18.1 and 50.0 cm² achieved certified PCEs of 19.3% and 19.2%, respectively (Fig. 3(d)). Furthermore, the reduced interfacial voids and carbohydrazide residuals at the buried layer stabilized the Pero-SCs and improved the yield of high-efficiency perovskite modules (Fig. 3(e)).
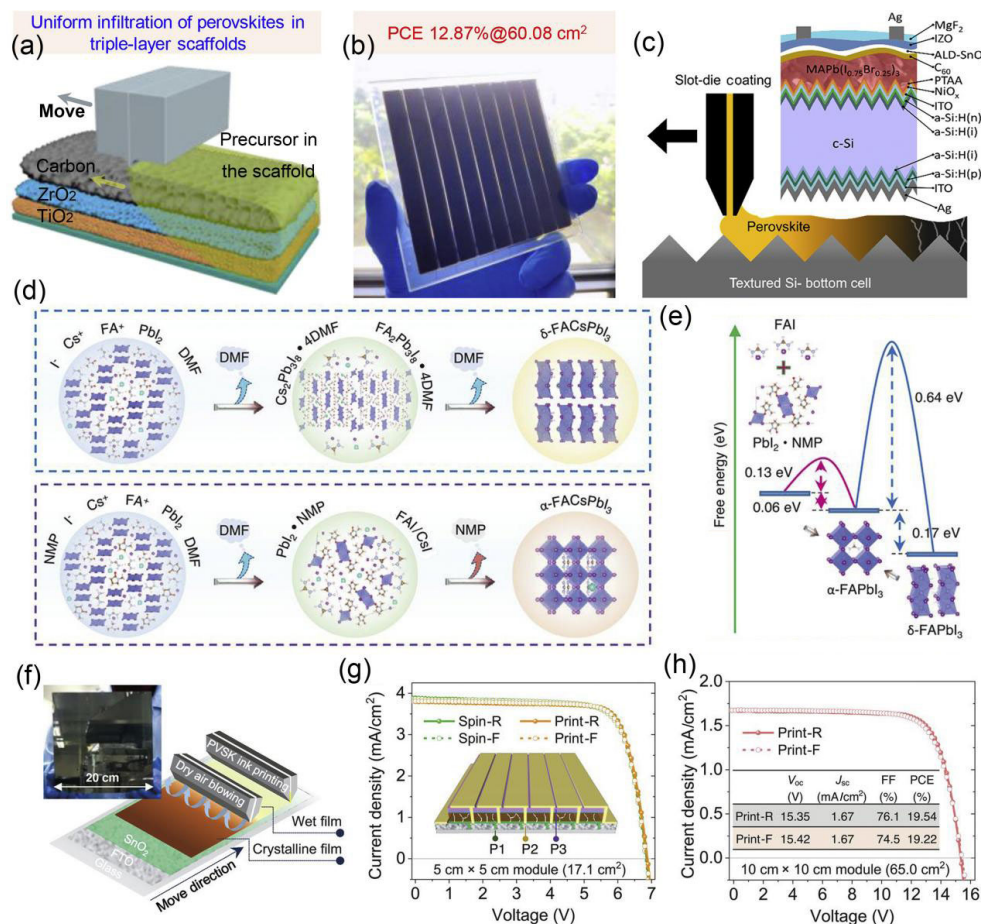
3.3 Slot-die coating

Slot-die coating is another ease-scalable industrial technology for film formation, which is highly mechanized. In this method, the ink is fed from a stored reservoir through a thin slit to extend over the substrate surface by the relative movement. During the coating process, the ink concentration does not change as it is sealed in a closed reservoir, which ensures the reproducibility of the working process. Moreover, the thickness of films can be controlled by the solution concentration, the distance of the coating head with the substrate, the movement speed, the feed speed of the storage pump, and substrate width. These attractive features promote that slot-die coating is the most potential industrial technology for depositing large-area perovskite films for PPMs.

In 2015, three-dimensional (3D) printer-based slot-die coater technique was used to fabricated 11.6%-efficiency PPMs with an active area of 47.3 cm² [41]. The MAPbI₃ perovskite films, ZnO electron transfer, and poly(3-hexylthiophene) (P3HT) hole transfer layers were all coated by slot-die with the assistance of air knife drying. For MAPbI₃ films, PbI₂ films were initially formed by slot-die coating, which was then

converted into MAPbI₃ film by dipping methylammonium iodide (MAI) solution. In 2017, the slot-die coated perovskite films were immediately dried by a vacuum chamber to promote 10.6% efficiency with good reproducibility of the carbon-electrode-based 5 cm × 5 cm module (active area of 17.3 cm²) [42]. In 2018, a PPM (active area of 168.75 cm²) on a 6-inch substrate was sheet-to-sheet produced by slot-die coating with remarkable efficiency of over 10% [43]. In 2020, Han's group employed slot-die coating to infiltrate the perovskite precursor into the TiO₂/ZrO₂/carbon scaffold, and PPMs with an active area of 60.08 cm² achieved a PCE of 12.87% (Figs. 4(a) and 4(b)) [44]. In the same year, textured silicon was utilized as the bottom cell to achieve the first slot-die-coated perovskite/silicon monolithic 2-terminal tandem with a PCE of 23.8% (Fig. 4(c)) [45].

In 2021, Cheng's group developed a crystallization strategy based on the lead halide template for slot-die FACsPbI₃ perovskite films [46], which exhibit better thermal stability and narrower optical bandgap compared with MAPbI₃ [16]. They proposed a two-step *in-situ* preparation strategy for the first time, which realized efficient and stable printing and preparation of photovoltaic modules (Fig. 4(f)). In the absence of methylammonium (MA) perovskite system, the formation of strong PbI₂·N-methylpyrrolidone (NMP) complex effectively induced the large-area dense and stable perovskite films (Figs. 4(d) and 4(e)). With adding NMP and excess PbCl₂, the intermediate phases with DMF and FA₂Pb₃I₈·4DMF product can be effectively restrained for the formation of PbI₂·NMP complex and PbX₂·0.5NMP·0.5DMF adduct, respectively, resulting in the translation of the dense and stable α-(FACs)PbI₃. Thus, the fast nucleation of PbI₂·NMP complex can effectively

Figure 4 (a) Schematic illustration for slot-die coating perovskite precursors on TiO_2/ZrO_2/carbon mesoporous scaffold. (b) Photograph image of the fabricated PPMs of 60.08 cm^2 area with efficiency of 12.87%. Reproduced with permission from Ref. [44], © Elsevier B.V. 2020. (c) Device architecture schematic of perovskite/silicon tandem devices with slot-die-coated perovskite films. Reproduced with permission from Ref. [45], © American Chemical Society 2020. (d) Schematic diagram of formamidinium lead triiodide ($FAPbI_3$) perovskite crystal growth with or without NMP. (e) Free-energy calculation for the formation of corresponding $FAPbI_3$ perovskites. (f) Schematic illustration for the slot-die printing of perovskite films with low-pressure dry air blowing. (g) Champion *J–V* curves of the 5 cm × 5 cm series-connected PPMs based on the spin-coating and slot-die printing methods (F: forward scan; R: reverse scan). (h) Champion *J–V* curves of the 10 cm×10 cm PPMs with the slot-die printed perovskite films. Reproduced with permission from Ref. [46], © Bu, T. L. et al. 2021.

suppress the δ-phase formation. Besides, KPF_6 was added into the perovskite precursor to eliminate the current hysteresis and further improve the PCE and stability of PPMs simultaneously. The KPF_6 addition has a passivation effect to reduce the defects for more stability. The unpackaged devices with 23% efficiency and excellent long-term thermal stability in ambient air (approximately 80% of the initial efficiency after aging at 85 °C for 500 h) can be achieved. The PCEs of slot printing modules with an effective area of 17.1 and 65.0 cm^2 were 20.42% (certified 19.3%) and 19.54%, respectively (Fig. 4). This study revealed the crystallization kinetics and regulation mechanism for controllably preparing perovskite films by solution method, which provides a novel strategy for industrial fabrication of PPMs.

3.4 Spray coating

Spray coating is a simple and low-cost depositing technique for large-area PPMs, in which the precursor solution droplets are sprayed by the gun pressure, spread across via the sheer force, and coalesce into wet films on the substrate. And the solvent evaporates in the wet film to leave a solid film [47]. Spray coating can be performed on various kinds of surfaces
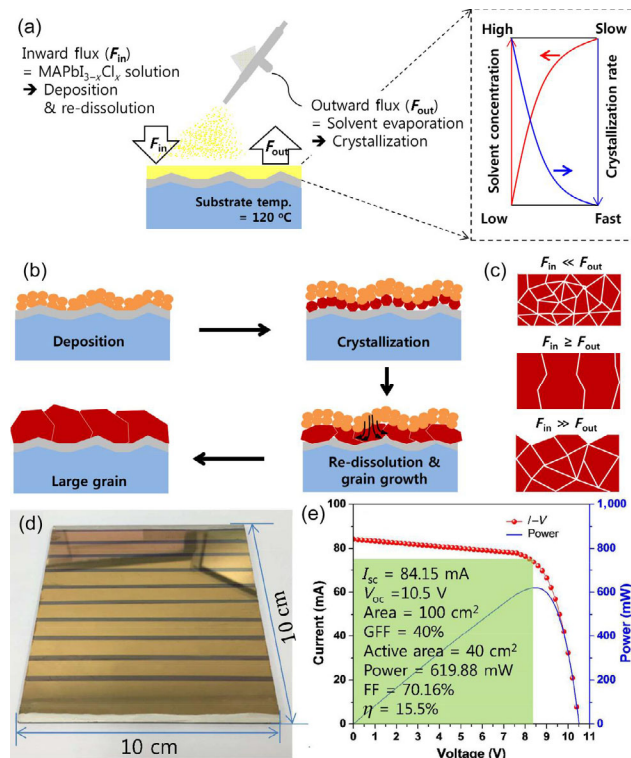
such as textured Si substrate due to the non-contact of the spray head and the substrate [48]. Spray coating is generally formulated at relatively low concentration ink to produce the perovskite films with desired thickness. If the solvent evaporates too quickly, the solution droplets have not enough time to spread for coalescing into uniform films. Conversely, if the drying process lasts for long, the wet film would shrink into poor-coverage films. Therefore, the regulation of spray coating perovskite films is a great challenge and the PCE of spray-coated devices is relatively low. Optimizing the spraying speed, substrate temperature, the distance between the nozzle and substrate, wet-film annealing temperature and time as well as the ink concentration, viscosity, and solvent flux can improve the film quality and thickness. It is important to note that possible escaping perovskite ink may contaminate the chamber and harm the experimental operators. The low utilization of the precursor solution is also a big barrier to this method toward commercialization. For fabricating PPMs, spray coating is easy to deposit charge transport layers, such as SnO_2 and NiO_x [49, 50], but difficult for perovskite films.

In 2014, spray coating was first used to deposit $MAPbI_{3−x}Cl_x$ films under ambient conditions for Pero-SCs [51]. The

substrate temperature, casting-solvent volatility, and annealing time and temperature of wet films can control the nucleation and crystallization, which were systemically explored in the morphology and coverage of the perovskite films. The relatively low substrate temperatures during solution deposition are correlated with perovskite films having a low substrate coverage because of the relatively-long drying time. As the substrate temperature is increased to 75 °C, the perovskite films become more continuous. The optimized device efficiency of 11% is relevant to the creation of dense films with surface coverage above 85%. In 2016, a dense $MAPbI_{3-x}Cl_x$ film composed of micron-sized grains was formed by controlling the re-dissolution and crystal grain growth [52]. There was a dynamic equilibrium by balancing the incoming (F_{in}) and outgoing solvent flux (F_{out}) of the evaporating solvent for spray coating perovskite films (Figs. 5(a)–5(c)). Finally, 10 cm × 10 cm modules (FTO/TiO$_2$/perovskite/spiro-OMeTAD/Au, active area of 40 cm^2) were created with an efficiency of 15.5% (Figs. 5(d) and 5(e)). More importantly, spray coating can be done at extremely high speed compared with other scalable techniques to achieve cost-effective, large-area, and efficient PPMs. Rolston and co-authors demonstrate rapid, air-ambient spray deposition of perovskite films at a rate of 12 m/min for efficient PPMs [53]. A heated substrate was coupled with ultrafast linear processing speeds to enable immunity to moisture ingress, even under high humidity conditions. A stable module power output of 18.0% was achieved.
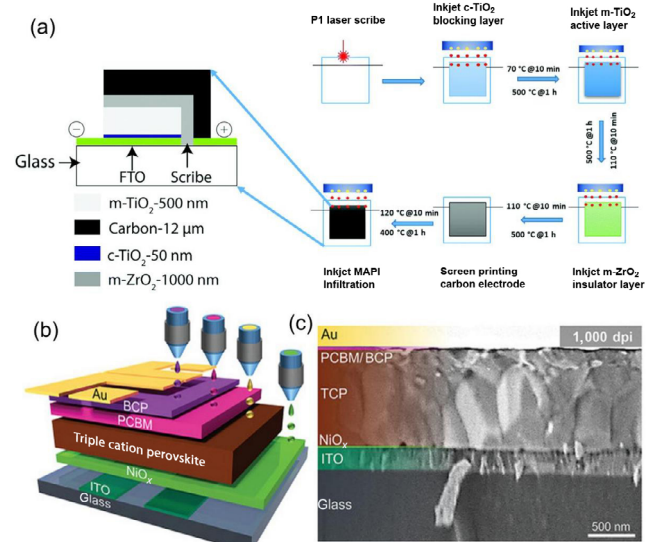
3.5 Inkjet printing

Inkjet printing is a digital method for coating films, where the precursor ink is pressed from a chamber through the printing head and patterned by a computer procedure. The inkjet printing can be performed in two models, such as continuous or selective dropping process. The perovskite ink is uniformly printed on the predesigned position by a digital procedure with the print nozzle relative motion on the substrate. The film thickness is finely affected by the size, movement speed and trajectory of the droplets through the nozzle, and the frequency and amplitude of the digital pulses [54]. The raw materials are highly utilized and multiple head printing can be realized to meet the needs of industrial production. In addition, this non-contact printing process is independent of special substrate morphology and materials. However, it is challenging to control the perovskite nucleation and crystal growth during the inject printing process to obtain high-quality films over a large area.

Inkjet printing is suitable for the large-area production of PPMs; however, it has been mainly reported to fabricate Pero-SCs. The metal oxide layers, i.e., c-TiO$_2$, m-TiO$_2$, and m-ZrO$_2$, as well as the perovskite precursor, were all injected and printed for carbon-based Pero-SCs [55]. The oxide layers and the carbon electrode were sintered at elevated temperature and then infiltrated with the perovskite ink by inkjet printing at room temperature (Fig. 6(a)). The carbon-based Pero-SCs with an area of 1.5 cm^2 achieved a PCE of 9.1%. Also p-i-n Pero-SCs were fabricated by inkjet printing the NiO$_x$ hole-transport layer, perovskite films, and electron-transport double layers of (6,6)-phenyl-C71-butyric acid methyl ester (PCBM) and bathocuproine (BCP) (Fig. 6(b)) [56]. The ink properties, inkjet parameters, and annealing procedure were all optimized for each layer with regard to the optical and electrical properties to promote an efficiency over of 17% with low hysteresis of the Pero-SCs. Given the fact that inkjet printing is a scalable technology, there are high prospects for printing large-area PPMs.

Figure 5 (a) Schematic illustration for the spray coating mechanism. (b) Crystalline grain growth of the perovskite film, and (c) balance between F_{in} and F_{out}. (d) Photograph images of the 10 cm × 10 cm module. (e) Photovoltaic properties. Reproduced with permission from Ref. [52], © Royal Society of Chemistry 2016.

Figure 6 (a) Device architecture with desired layer thicknesses. Process flow demonstrating inkjet-printed compact TiO$_2$ layer, mesoporous TiO$_2$ layer, mesoporous ZrO$_2$ layer and infiltration of perovskite precursor. Yellow dots represent the print head nozzles while red dots represent the ejected droplets. Reproduced with permission from Ref. [55], © The Royal Society of Chemistry 2020. (b) Schematic of the device architecture with indium tin oxide (ITO), printed NiO$_x$, perovskite, PCBM and BCP layers. (c) Cross-sectional SEM image of the device. Reproduced with permission from Ref. [56], © Schackmar, F., et al. 2020.

3.6 Soft-cover deposition

In 2016, Han's group first introduced the soft-cover deposition for perovskite films in ambient air, where the surface wettability, solution viscosity, and thermal crystallization are the key factors for the film quality [57]. At first, a substrate is preheated on a hotplate, and then a certain amount of perovskite ink is dropped onto the substrate. Then a soft flexible piece is covered in the liquid precursor, which can drive the precursor ink to spread up for films due to the superior surface wettability (Fig. 7(a)). In addition, the perovskite ink is stable on the preheated substrate even at the solution boiling point because the soft cover blocks the solvent evaporation from the thin liquid film into the air. Then the soft piece is peeled off by the programmed mechanical hand, and one side is clenched and moved to the other at a certain speed. Once the solution is exposed to the air, the solvent starts to evaporate and the crystallization of perovskite films occurs simultaneously. They deposited large-area perovskite films (51 cm^2) with large crystal grains and without pinholes and rough borders. Highly reproducible PCE up to 17.6% was achieved in unit cells (FTO/NiO/MAPbI$_3$/PCBM/BCP/Ag) with 1 cm^2 effective area. Later on, they fabricated 36 cm^2 PPMs with a PCE of 12.07%, which has been certified by the National Institute of Advanced Industrial Science and Technology.

In 2017, Han et al. used low-temperature soft-cover deposition for perovskite films, where the thermal convection-induced defects are eliminated through a strategy of surface tension relaxation [58]. They deposited compact, homogeneous, and convection-induced-defects-free perovskite films with an area of 12 cm^2, which enables a PCE up to 15.5% on one cell with the effective area of 5 cm^2. The flexible solar cell was also fabricated with a PCE of 15.3%. Later on, they produced a novel type of yellow transparent perovskite precursor by mixing the CH$_3$NH$_3$I-3CH$_3$NH$_2$ transparent liquid and PbI$_2$-CH$_3$NH$_2$ colloid, which were prepared by direct reaction between CH$_3$NH$_3$I (and PbI$_2$) powder and CH$_3$NH$_2$ gas [59]. Then, they developed the soft-cover deposition for perovskite films using the above solvent-free perovskite precursor, in which there are mainly three steps: (I) add amine complex precursors and cover with the PI film; (II) apply pressure; (III) heat and peel
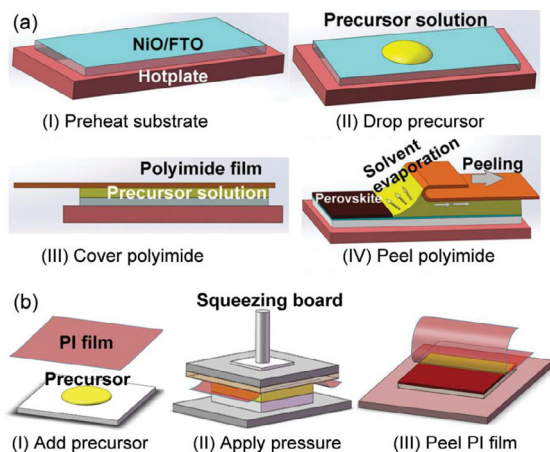
Figure 7 (a) Schematic illustration for the soft-cover deposition with four steps: (I) preheat the substrate, (II) drop the precursor, (III) cover the polyimide (PI) film, and (IV) peel the PI film. Reproduced with permission from Ref. [57], © The Royal Society of Chemistry 2016. (b) Schematic illustration for the developed soft-cover deposition with pressure processing for perovskite films [59].

off the PI film (Fig. 7(b)). The mesoporous TiO$_2$-based modules with the aperture areas of 17.6 and 36.1 cm^2 achieved efficiencies up to 15.8% and 13.9%, respectively. This work paves a novel way for the solvent- and vacuum-free soft-cover deposition of uniform perovskite films for PPMs on a large scale.

3.7 Vapor deposition

Vapor evaporation such as dual-source [60], single-source evaporation [61], and chemical vapor deposition [62], has been successfully used to deposit perovskite films with uniformity and reproducibility. The perovskite films can be managed by the organic salt component, vapor pressure, reaction rate, and post-treatment. Importantly, the vapor evaporation can finely control film thickness, which enables film uniformity for flexible devices and optimization of optical properties for tandem devices [62–64]. In 2013, Snaith et al. initially used this method to deposit CH$_3$NH$_3$PbI$_{3-x}$Cl$_x$ films for Pero-SCs with a PCE of 15.4% [60]. Liu's group deposited large-area perovskite films with superior uniformity and excellent quality on 300 cm^2 flexible substrates [62]. In 2020, an all-evaporation technique was developed for both perovskite films and the hole-transporting layer to achieve 13.15% PCE of the flexible perovskite solar module (active area of 16.0 cm^2) [63]. However, the cost is higher than that of the solution method, especially the expensive vacuum equipment, which limits the widespread application of vapor deposition for large-area PPMs.

In the hybrid chemical vapor deposition, the inorganic precursor films (e.g., PbI$_2$, PbCl$_2$, and CsI) are first deposited by a large-area deposition method, and then transformed into perovskite films in the vapor of organic amine halide (e.g., formamidinium iodide (FAI), methylammonium iodide (MAI), and methylammonium bromide (MABr)). However, the conventional process needs several hours, which increases the fabrication cost. Moreover, the long-time deposition has a detrimental effect on the oxide buried layers, which is unfavorable for the device performance [65]. Qi's group has developed rapid hybrid chemical vapor deposition for large-area perovskite films toward PPMs. In Step 1, a crucible containing the organic compound and substrate with pre-coated inorganic layer was loaded into a single-zone quartz tube; in Step 2, the carrier gas flowed and the vacuum was kept at a pressure of 10 torr; in Step 3 the infrared (IR) heating system was slid to enclose both the organic powder and substrate and followed by the starting the IR heating system; in Step 4 after the heating process is finished, the IR heating system is turned off and the cooling system is turned on (Fig. 8(a)). They significantly reduced the deposition time to less than 10 min, comparable with the typical solution process. The PPMs with a designated area of 22.4 cm^2 (Fig. 8(b)) achieved an efficiency of 12.3% without obvious hysteresis (Fig. 8(c)), and maintained 90% of the initial value with continuous operation after 800 h in a dry N$_2$ box (Fig. 8(d)) [66].

4 Serial and parallel interconnected PPMs

In manufacturing PPMs, the consisting layers need to be patterned for the interconnection of individual cells. Figure 9 shows the cross-sectional diagram of serial and parallel interconnected PPMs. To date, the series of interconnected PPMs were more frequently studied as compared to parallel ones. In the serially interconnected architectures (Fig. 9(a)), there are mainly three scribes P1, P2, and P3. P1 scribe is defined as the etched lines of the transparent conductive layers,
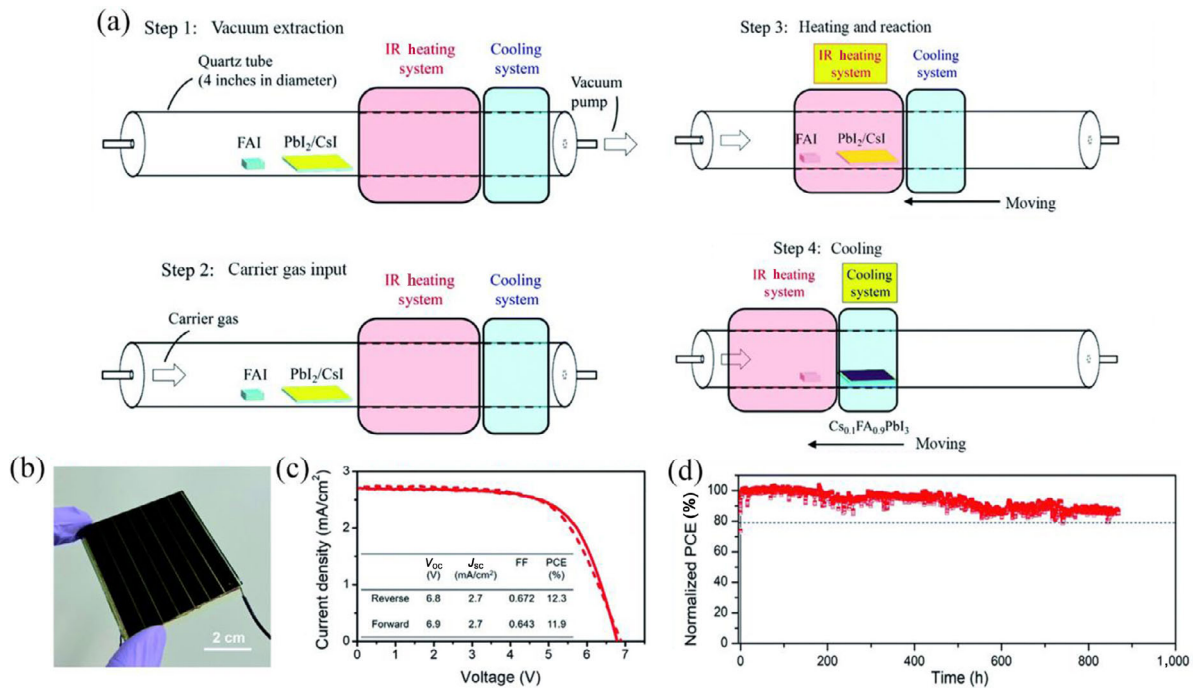
Figure 8 (a) Schematic illustrations showing the steps and major features for fabricating perovskite films via the RHCVD method. The cooling system is slid to the substrate position. (b) Photograph image of the 5 cm × 5 cm module. (c) *I–V* curve of forward and reverse scan from the optimized PPM with the efficiency of 12.3%. (d) Long-term operational stability of PPMs under simulated 1-sun illumination. Reproduced with permission from Ref. [66], © The Royal Society of Chemistry 2020.

such as ITO and FTO. P2 scribe is the selectively etched lines of active layer (electron transport (n), transport hole (p), and perovskite layers). And P3 scribe is the patterned lines of the back electrode (such as Ag and Au). The dead area is related to the three scribes, and the effect can be quantified by the geometric fill factor (GFF) as following

$$GFF = \frac{Active\ area}{Active\ area + Dead\ area} \times 100\%$$

The parallel interconnected PPM consists of two scribes of P1 and P2 lines. P1 is the patterned line separated by two electrodes, similar to the one cell. P2 is the etched lines of active layers and the conductive electrode, similar to the P3 of serially interconnected architectures, as shown in Fig. 9(b). The conductive girds are connected to form parallel interconnections.

Series and parallel connected modules are characterized by high voltage with low current, and low voltage with high current, respectively. For practical application, a number of series and parallel connected modules are taken to form a solar array for the desired voltage and current level. Notably, a reasonable and logical dividing piece and module design are critical for the high efficiency and stability of PPMs. In 2019, Yang's group discussed the influence of the length and width on the output performance when device areas were increased and design of series and parallel connection for large-area PPMs [67]. High efficiencies of 19.52% and 18.65% are obtained for single cells based on areas of 0.1 and 1.0 cm^2, respectively. When the device area is increased, increasing the length of the device can achieve a higher efficiency than increasing the width for single cells. Comparing series and parallel connection mode, the first series and then parallel connection of PPMs is the best way to obtain a high power output. The design study offers a direction for PPMs in future applications.
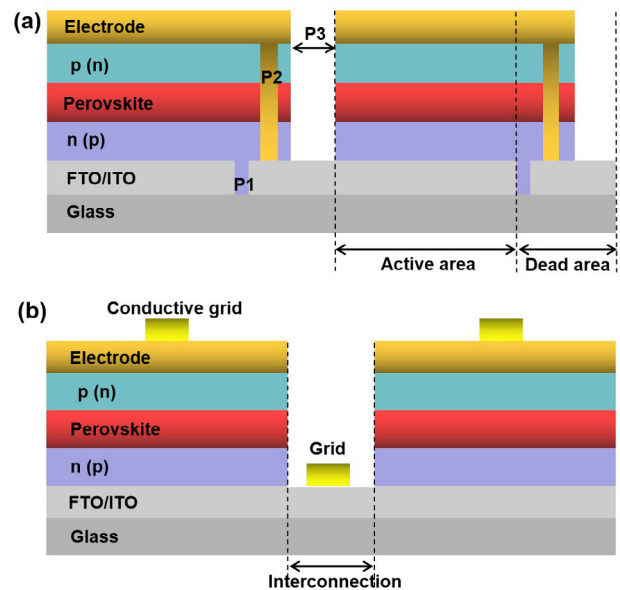
Figure 9 Cross-sectional schematic diagrams of grid lines. The sub-cells are connected in series (a) or parallel (b).

5 Stability of PPMs

The stability of PPMs is one of the most challenges that needs to be addressed for commercial applications. The long-term stability of small-area Pero-SCs has reached about one year, far below 25 years of silicon cells [68]. To date, a series of strategies have been adopted to improve the device stability, such as grain boundary passivation [69], interface/stress engineering [70–73], low dimension structure [68, 74, 75], and device encapsulation [76]. Here, the degradation of PPMs will be highlighted to analyze the module stability issue with

the relative scribes [77]. Among the three scribes in parallel architectures, the P2 scribe has the most influence on the device stability. Firstly, the laser energy leads to the local degradation of the perovskite film during the P2 etching [78]. Secondly, if the P2 scribe is not thoroughly removed, there is additional shunt resistance at interconnections, which can accelerate potential-induced degradation [79, 80]. Thirdly, impurities may degrade perovskite films due to an unclean etching environment. And the possible lateral contact between perovskite and metal electrodes reduces the stability of the PPMs [81]. Furthermore, the degraded lead halide compounds can further diffuse from the P2 scribe into the perovskite area [82]. Besides, as for etching the P3 scribe, the exposed environment may destroy the perovskite layer again. It should be noted that the encapsulation can improve the device stability, but the encapsulation materials in the P3 scribe may react with the perovskite structures [81].

The compact layer of TiO_2 through high-temperature annealing is difficult to be etched thoroughly and can be replaced by a low-temperature-treated n-type layer to avoid the incomplete P2 scribes [76, 83]. To avoid the direct contact between perovskite and metal back electrode inside of the P2 scribe, a diffusion barrier was proposed [81] and a series of low dimensional materials were chosen as diffusion barriers, such as chemically and thermally stable zero-dimensional (0D) Al_2O_3 nanoparticles, one-dimensional (1D) polydimethylsiloxane (PDMS), and two-dimensional (2D) C_3N_4 (Fig. 10). After the P2 scribe is filled with the diffusion barrier material, an additional laser scribe should be taken inside of the original P2 to create a protective layer. The leakage rate of iodide was reduced by 10^3–10^7 times, and the non-radiation recombination at the perovskite surface was also reduced due to the defect passivation of the diffusion barriers. A stable PPM at an aperture area of 36 cm^2 had an efficiency of 15.6%, which maintained 95% of the initial value after being baked 1,000 h at 85 °C and 91% after 1,000 h under the maximum power point tracking.
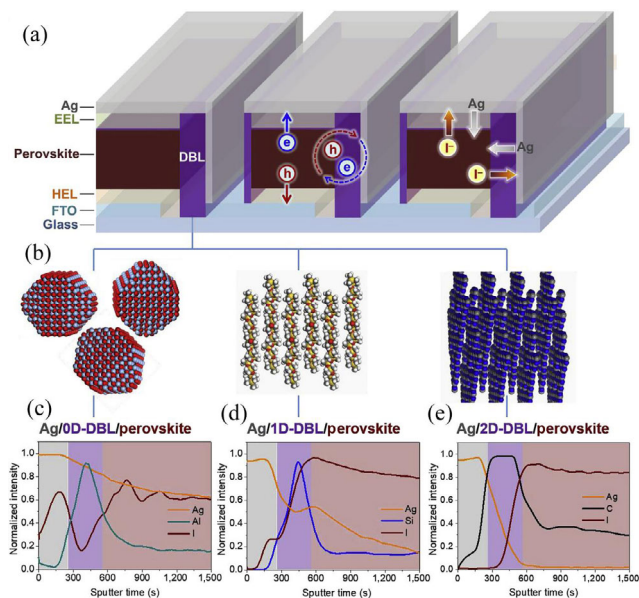
Figure 10 (a) Schematic illustration of diffusion barrier layer (DBL) in PPMs. (b) 0D Al_2O_3 nanoparticles, 1D PDMS, and 2D C_3N_4 for DBL. (c)–(e) The depth profiles of diffused iodide and Ag in Ag/0D (1D, 2D)-DBL/perovskite films with aluminum, silicon and carbon signals, respectively. Reproduced with permission from Ref. [81], © Elsevier B.V. 2019.

6 Summary and future outlook

This review covered various coating methods for large-area perovskite films, including spin coating, doctor blading, slot-die coating, spray coating, inkjet printing, soft-cover deposition, and vapor deposition, indicated their limitations and provided an outlook. The technical characteristics have been comprehensively discussed as well as the growth of high-quality perovskite films for large-area modules. For future commercialization, the following development directions should be worth noting:

(I) The coating methods should be continued to develop for the large-area high-quality perovskite films accompanied by nucleation and growth control, and the perovskite compositions should be further optimized to enhance the efficient PPMs.

(II) The buried and surface layers should be simultaneously modified to passivate the perovskite defects in PPMs, in which the enhanced band alignment can accelerate charge transfer. Besides, the corrosion reaction by permeating the perovskite components into metal electrodes should be also solved by interface layers.

(III) The stability strategies have been widely used in small-area Pero-SCs. Those strategies should be referenced and coordinated to greatly improve the stability of large-area PPMs.

Acknowledgements

Declaration of conflicting interests

The authors declare no conflicting interests regarding the content of this article.

References

[1] National Renewable Energy Laboratory. *Best research-cell efficiency chart* [Online]. 2022. https://www.nrel.gov/pv/cell-efficiency.html (accessed 24 June 2022).

[2] Chu, L. Pseudohalide anion engineering for highly efficient and stable perovskite solar cells. *Matter* **2021**, *4*, 1762–1764.

[3] Lee, M. M.; Teuscher, J.; Miyasaka, T.; Murakami, T. N.; Snaith, H. J. Efficient hybrid solar cells based on meso-superstructured organometal halide perovskites. *Science* **2012**, *338*, 643–647.

[4] Lei, Y.; Li, Y.; Lu, C.; Yan, Q.; Wu, Y.; Babbe, F.; Gong, H.; Zhang, S.; Zhou, J. et al. Perovskite superlattices with efficient carrier dynamics, *Nature* **2022**, *608*, 317323.

[5] Li, Z.; Li, B.; Wu, X.; Sheppard, S. A.; Zhang, S. F.; Gao, D. P.; Long, N. J.; Zhu, Z. L. Organometallic-functionalized interfaces for highly efficient inverted perovskite solar cells. *Science* **2022**, *376*, 416–420.

[6] Yang, J.; Chu, L.; Hu, R. Y.; Liu, W.; Liu, N. J.; Ma, Y. H.; Ahmad, W.; Li, X. A. Work function engineering to enhance open-circuit voltage in planar perovskite solar cells by g-C_3N_4 nanosheets. *Nano Res.* **2021**, *14*, 2139–2144.

[7] Li, X.; Bi, D. Q.; Yi, C. Y.; Décoppet, J. D.; Luo, J. S.; Zakeeruddin, S. M.; Hagfeldt, A.; Grätzel, M. A vacuum flash-assisted solution process for high-efficiency large-area perovskite solar cells. *Science* **2016**, *353*, 58–62.

[8] Li, Z.; Wang, X.; Wang, Z; Shao, Z.; Hao, L.; Rao, Y.; Chen, C.; Liu, D.; Zhao, Q.; Sun, X. et al. Ammonia for post-healing of formamidinium-based perovskite films. *Nat. Commun.* **2022**, *13*, 4417.

[9] National Renewable Energy Laboratory (NREL). Champion photovoltaic module efficiency chart [Online]. 2022. https://www.nrel.gov/pv/module-efficiency.html (accessed 24 June 2022).

[10] Li, C. P.; Yin, J.; Chen, R. H.; Lv, X. D.; Feng, X. X.; Wu, Y. Y.; Cao, J. Monoammonium porphyrin for blade-coating stable large-area perovskite solar cells with > 18% efficiency. *J. Am. Chem. Soc.* **2019**, *141*, 6345–6351.

[11] Liu, X. H.; Chen, M.; Zhang, Y.; Xia, J. X.; Yin, J. Z.; Li, M.; Brooks, K. G.; Hu, R. Y.; Gao, X. X.; Kim, Y. H. et al. High-efficiency perovskite photovoltaic modules achieved via cesium doping. *Chem. Eng. J.* **2022**, *431*, 133713.

[12] Chu, L.; Liu, W.; Qin, Z. F.; Zhang, R.; Hu, R. Y.; Yang, J.; Yang, J. P.; Li, X. A. Boosting efficiency of hole conductor-free perovskite solar cells by incorporating p-type NiO nanoparticles into carbon electrodes. *Sol. Energy Mater. Sol. Cells* **2018**, *178*, 164–169.

[13] Liu, N. J.; Chu, L.; Ahmad, W.; Hu, R. Y.; Luan, R. F.; Liu, W.; Yang, J.; Ma, Y. H.; Li, X. A. Low-pressure treatment of CuSCN hole transport layers for enhanced carbon-based perovskite solar cells. *J. Power Sources* **2021**, *499*, 229970.

[14] Zhu, J; Qian, Y; Li. Z; Gong, O. Y.; An, Z.; Liu, Q.; Choi, J. H.; Guo, H.; Yoo, P. J.; Kim, D. H. et al. Defect healing in FAPb(I$_{1−x}$Br$_x$)$_3$ perovskites: Multifunctional fluorinated sulfonate surfactant anchoring enables > 21% modules with improved operation stability. *Adv. Energy Mater* **2022**, *12*, 2200632.

[15] Kim, Y. Y.; Yang, T. Y.; Suhonen, R.; Kemppainen, A.; Hwang, K.; Jeon, N. J.; Seo, J. Roll-to-roll gravure-printed flexible perovskite solar cells using eco-friendly antisolvent bathing with wide processing window. *Nat. Commun.* **2020**, *11*, 5146.

[16] Turren-Cruz, S. H.; Hagfeldt, A.; Saliba, M. Methylammonium-free, high-performance, and stable perovskite solar cells on a planar architecture. *Science* **2018**, *362*, 449–453.

[17] Chu, L.; Ding, L. Self-assembled monolayers in perovskite solar cell. *J. Semiconductors*, **2021**, *42*, 090202.

[18] Thanh, N. T. K.; Maclean, N.; Mahiddine, S. Mechanisms of nucleation and growth of nanoparticles in solution. *Chem. Rev.* **2014**, *114*, 7610–7630.

[19] Sugimoto, T.; Shiba, F.; Sekiguchi, T.; Itoh, H. Spontaneous nucleation of monodisperse silver halide particles from homogeneous gelatin solution I: Silver chloride. *Colloids Surf. A: Physicochem. Eng. Aspects* **2000**, *164*, 183–203.

[20] Jeon, N. J.; Noh, J. H.; Kim, Y. C.; Yang, W. S.; Ryu, S.; Seok, S. I. Solvent engineering for high-performance inorganic–organic hybrid perovskite solar cells. *Nat. Mater.* **2014**, *13*, 897–903.

[21] Lee, J. W.; Lee, D. K.; Jeong, D. N.; Park, N. G. Control of crystal growth toward scalable fabrication of perovskite solar cells. *Adv. Funct. Mater.* **2019**, *29*, 1807047.

[22] Zeng, L. X.; Chen, S.; Forberich, K.; Brabec, C. J.; Mai, Y. H.; Guo, F. Controlling the crystallization dynamics of photovoltaic perovskite layers on larger-area coatings. *Energy Environ. Sci.* **2020**, *13*, 4666–4690.

[23] Abraham, F. F. *Homogeneous Nucleation Theory*; Academic Press: New York, 1974.

[24] Lee, K. M.; Lin, C. J.; Liou, B. Y.; Yu, S. M.; Hsu, C. C.; Suryanarayanan, V.; Wu, M. C. Selection of anti-solvent and optimization of dropping volume for the preparation of large area sub-module perovskite solar cells. *Sol. Energy Mater. Sol. Cells* **2017**, *172*, 368–375.

[25] Xu, Y. B.; Wang, S. B.; Gu, L. L.; Yuan, N. Y.; Ding, J. N. Structural design for efficient perovskite solar modules. *Sol. RRL* **2021**, *5*, 2000733.

[26] Küffner, J.; Wahl, T.; Schultes, M.; Hanisch, J.; Zillner, J.; Ahlswede, E.; Powalla, M. Nanoparticle wetting agent for gas stream-assisted blade-coated inverted perovskite solar cells and modules. *ACS Appl. Mater. Interfaces* **2020**, *12*, 52678–52690.

[27] Xu, Z.; Zeng, L.; Hu, J.; Wang, Z.; Zhang, P.; Brabec, C. J.; Forberich, K.; Mai, Y.; Guo. F. Reducing energy barrier of δ-to-α phase transition for printed formamidinium lead iodide photovoltaic devices. *Nano Energy* **2022**, *91*, 106658.

[28] Im, J. H.; Kim, H. S.; Park, N. G. Morphology-photovoltaic property correlation in perovskite solar cells: One-step versus two-step deposition of CH$_3$NH$_3$PbI$_3$. *APL Mater.* **2014**, *2*, 081510.

[29] Han, G. S.; Kim, J.; Bae, S.; Han, S.; Kim, Y. J.; Gong, O. Y.; Lee, P.; Ko, M. J.; Jung, H. S. Spin-coating process for 10 cm × 10 cm perovskite solar modules enabled by self-assembly of SnO$_2$ nanocolloids. *ACS Energy Lett.* **2019**, *4*, 1845–1851.

[30] Bu, T. L.; Liu, X. P.; Li, J.; Huang, W. C.; Wu, Z. L.; Huang, F. Z.; Cheng, Y. B.; Zhong, J. Dynamic antisolvent engineering for spin coating of 10 × 10 cm^2 perovskite solar module approaching 18%. *Sol. RRL* **2020**, *4*, 1900263.

[31] Zhao, P. J.; Kim, B. J.; Ren, X. D.; Lee, D. G.; Bang, G. J.; Jeon, J. B.; Kim, W. B.; Jung, H. S. Antisolvent with an ultrawide processing window for the one-step fabrication of efficient and large-area perovskite solar cells. *Adv. Mater.* **2018**, *30*, 1802763.

[32] Liu, C.; Yang, Y.; Rakstys, K.; Mahata, A.; Franckevicius, M.; Mosconi, E.; Skackauskaite, R.; Ding, B.; Brooks, K. G.; Usiobo, O. J. et al. Tuning structural isomers of phenylenediammonium to afford efficient and stable perovskite solar cells and modules. *Nat. Commun.* **2021**, *12*, 6394.

[33] Kim, J. H.; Williams, S. T.; Cho, N.; Chueh, C. C.; Jen, A. K. Y. Enhanced environmental stability of planar heterojunction perovskite solar cells based on blade-coating. *Adv. Energy Mater.* **2015**, *5*, 1401229.

[34] Yang, M. J.; Li, Z.; Reese, M. O.; Reid, O. G.; Kim, D. H.; Siol, S.; Klein, T. R.; Yan, Y. F.; Berry, J. J.; van Hes, M. F. A. M. et al. Perovskite ink with wide processing window for scalable high-efficiency solar cells. *Nat. Energy* **2017**, *2*, 17038.

[35] Deng, Y. H.; Zheng, X. P.; Bai, Y.; Wang, Q.; Zhao, J. J.; Huang, J. S. Surfactant-controlled ink drying enables high-speed deposition of perovskite films for efficient photovoltaic modules. *Nat. Energy* **2018**, *3*, 560–566.

[36] Deng, Y. H.; Van Brackle, C. H.; Dai, X. Z.; Zhao, J. J.; Chen, B.; Huang, J. S. Tailoring solvent coordination for high-speed, room-temperature blading of perovskite photovoltaic films. *Sci. Adv.* **2019**, *5*, aax7537.

[37] Dai, X. Z.; Deng, Y. H.; Van Brackle, C. H.; Chen, S. S.; Rudd, P. N.; Xiao, X.; Lin, Y.; Chen, B.; Huang, J. S. Scalable fabrication of efficient perovskite solar modules on flexible glass substrates. *Adv. Energy Mater.* **2020**, *10*, 1903108.

[38] Chen, B.; Yu, Z. J.; Manzoor, S.; Wang, S.; Weigand, W.; Yu, Z. H.; Yang, G.; Ni, Z. Y.; Dai, X. Z.; Holman, Z. C. et al. Blade-coated perovskites on textured silicon for 26%-efficient monolithic perovskite/silicon tandem solar cells. *Joule* **2**020, *4*, 850–864.

[39] Chen, S. S.; Dai, X. Z.; Xu, S.; Jiao, H. Y.; Zhao, L.; Huang, J. S. Stabilizing perovskite-substrate interfaces for high-performance perovskite modules. *Science* **2021**, *373*, 902–907.

[40] Deng, Y. H.; Wang, Q.; Yuan, Y. B.; Huang, J. S. Vividly colorful hybrid perovskite solar cells by doctor-blade coating with perovskite photonic nanostructures. *Mater. Horiz.* **2015**, *2*, 578–583.

[41] Vak, D.; Hwang, K.; Faulks, A.; Jung, Y. S.; Clark, N.; Kim, D. Y.; Wilson, G. J.; Watkins, S. E. 3D printer based slot-die coater as a lab-to-fab translation tool for solution-processed solar cells. *Adv. Energy Mater.* **2015**, *5*, 1401539.

[42] Cai, L. H.; Liang, L. S.; Wu, J. F.; Ding, B.; Gao, L. L.; Fan, B. Large area perovskite solar cell module. *J. Semicond.* **2017**, *38*, 014006.

[43] Di Giacomo, F.; Shanmugam, S.; Fledderus, H.; Bruijnaers, B. J.; Verhees, W. J. H.; Dorenkamper, M. S.; Veenstra, S. C.; Qiu, W. M.; Gehlhaar, R.; Merckx, T. et al. Up-scalable sheet-to-sheet production of high efficiency perovskite module and solar cells on 6-in. substrate using slot die coating. *Sol. Energy Mater. Sol. Cells* **2018**, *181*, 53–59.

[44] Xu, M.; Ji, W. X.; Sheng, Y. S.; Wu, Y. W.; Cheng, H.; Meng, J.; Yan, Z. B.; Xu, J. F.; Mei, A. Y.; Hu, Y. et al. Efficient triple-mesoscopic perovskite solar mini-modules fabricated with slot-die coating. *Nano Energy* **2020**, *74*, 104842.

[45] Subbiah, A. S.; Isikgor, F. H.; Howells, C. T.; De Bastiani, M.; Liu, J.; Aydin, E.; Furlan, F.; Allen, T. G.; Xu, F. Z.; Zhumagali, S. et al. High-performance perovskite single-junction and textured perovskite/silicon tandem solar cells via slot-die-coating. *ACS Energy Lett.* **2020**, *5*, 3034–3040.

[46] Bu, T. L.; Li, J.; Li, H. Y.; Tian, C. C.; Su, J.; Tong, G. Q.; Ono, L. K.; Wang, C.; Lin, Z. P.; Chai, N. Y. et al. Lead halide-templated crystallization of methylamine-free perovskite for efficient photovoltaic modules. *Science* **2021**, *372*, 1327–1332.

[47] Uličná, S.; Dou, B. J.; Kim, D. H.; Zhu, K.; Walls, J. M.; Bowers, J. W.; Van Hest, M. F. A. M. Scalable deposition of high-efficiency perovskite solar cells by spray-coating. *ACS Appl. Energy Mater.* **2018**, *1*, 1853–1857.

[48] Sansoni, S.; De Bastiani, M.; Aydin, E.; Ugur, E.; Isikgor, F. H.; Al-Zahrani, A.; Lamberti, F.; Laquai, F.; Meneghetti, M.; De Wolf, S. Eco-friendly spray deposition of perovskite films on macroscale textured surfaces. *Adv. Mater. Technol.* **2020**, *5*, 1901009.

[49] Chou, L. H.; Yu, Y. T.; Osaka, I.; Wang, X. F.; Liu, C. L. Spray deposition of NiO$_x$ hole transport layer and perovskite photoabsorber in fabrication of photovoltaic mini-module. *J. Power Sources* **2021**, *491*, 229586.

[50] Taheri, B.; Calabrò, E.; Matteocci, F.; Di Girolamo, D.; Cardone, G.; Liscio, A.; Di Carlo, A.; Brunetti, F. Automated scalable spray coating of SnO$_2$ for the fabrication of low-temperature perovskite solar cells and modules. *Energy Technol.* **2020**, *8*, 1901284.

[51] Barrows, A. T.; Pearson, A. J.; Kwak, C. K.; Dunbar, A. D. F.; Buckley, A. R.; Lidzey, D. G. Efficient planar heterojunction mixed-halide perovskite solar cells deposited via spray-deposition. *Energy Environ. Sci.* **2014**, *7*, 2944–2950.

[52] Heo, J. H.; Lee, M. H.; Jang, M. H.; Im, S. H. Highly efficient CH$_3$NH$_3$PbI$_{3-x}$Cl$_x$ mixed halide perovskite solar cells prepared by re-dissolution and crystal grain growth via spray coating. *J. Mater. Chem. A* **2016**, *4*, 17636–17642.

[53] Rolston, N.; Scheideler, W. J.; Flick, A. C.; Chen, J. P.; Elmaraghi, H.; Sleugh, A.; Zhao, O.; Woodhouse, M.; Dauskardt, R. H. Rapid open-air fabrication of perovskite solar modules. *Joule* **2020**, *4*, 2675–2692.

[54] Cheng, Y. J.; Wu, H. J.; Ma, J. J.; Li, P. W.; Gu, Z. K.; Zang, S. Q.; Han, L. Y.; Zhang, Y. Q.; Song, Y. L. Droplet manipulation and crystallization regulation in inkjet-printed perovskite film formation. *CCS Chem.* **2022**, *4*, 1465–1485.

[55] Verma, A.; Martineau, D.; Abdolhosseinzadeh, S.; Heier, J.; Nüesch, F. Inkjet printed mesoscopic perovskite solar cells with custom design capability. *Mater. Adv.* **2020**, *1*, 153–160.

[56] Schackmar, F.; Eggers, H.; Frericks, M.; Richards, B. S; Lemmer, U.; Hernandez-Sosa, G.; Paetzold, U. W. Perovskite solar cells with all-inkjet-printed absorber and charge transport layers. *Adv. Mater. Technol.* **2021**, *6*, 2000271.

[57] Ye, F.; Chen, H.; Xie, F. X.; Tang, W. T.; Yin, M. S.; He, J. J.; Bi, E. B.; Wang, Y. B.; Yang, X. D.; Han, L. Y. Soft-cover deposition of scaling-up uniform perovskite thin films for high cost-performance solar cells. *Energy Environ. Sci.* **2016**, *9*, 2295–2301.

[58] Ye, F.; Tang, W. T.; Xie, F. X.; Yin, M. S.; He, J. J.; Wang, Y. B.; Chen, H.; Qiang, Y. H.; Yang, X. D.; Han, L. Y. Low-temperature soft-cover deposition of uniform large-scale perovskite films for high-performance solar cells. *Adv. Mater.* **2017**, *29*, 1701440.

[59] Chen, H.; Ye, F.; Tang, W. T.; He, J. J.; Yin, M. S.; Wang, Y. B.; Xie, F. X.; Bi, E. B.; Yang, X. D.; Grätzel, M. et al. A solvent- and vacuum-free route to large-area perovskite films for efficient solar modules. *Nature* **2017**, *550*, 92–95.

[60] Liu, M. Z.; Johnston, M. B.; Snaith, H. J. Efficient planar heterojunction perovskite solar cells by vapour deposition. *Nature* **2013**, *501*, 395–398.

[61] Shen, P. S.; Chen, J. S.; Chiang, Y. H.; Li, M. H.; Guo, T. F.; Chen, P. Low-pressure hybrid chemical vapor growth for efficient perovskite solar cells and large-area module. *Adv. Mater. Interfaces* **2016**, *3*, 1500849.

[62] Feng, J. S.; Jiao, Y. X.; Wang, H.; Zhu, X. J.; Sun, Y. M.; Du, M. Y.; Cao, Y. X.; Yang, D.; Liu, S. F. High-throughput large-area vacuum deposition for high-performance for mamidine-based perovskite solar cells. *Energy Environ. Sci.* **2021**, *14*, 3035–3043.

[63] Lei, T.; Li, F. H.; Zhu, X. Y.; Dong, H.; Niu, Z. W.; Ye, S. W.; Zhao, W.; Xi, J.; Jiao, B.; Ding, L. M. et al. Flexible perovskite solar modules with functional layers fully vacuum deposited. *Sol. RRL* **2020**, *4*, 2000292.

[64] Forgács, D.; Gil-Escrig, L.; Pérez-Del-Rey, D.; Momblona, C.; Werner, J.; Niesen, B.; Ballif, C.; Sessolo, M.; Bolink, H. J. Efficient monolithic perovskite/perovskite tandem solar cells. *Adv. Energy Mater.* **2017**, *7*, 1602121.

[65] Qiu, L. B.; He, S. S.; Jiang, Y.; Son, D. Y.; Ono, L. K.; Liu, Z. H.; Kim, T.; Bouloumis, T.; Kazaoui, S.; Qi, Y. B. Hybrid chemical vapor deposition enables scalable and stable Cs-FA mixed cation perovskite solar modules with a designated area of 91.8 cm^2 approaching 10% efficiency. *J. Mater. Chem. A* **2019**, *7*, 6920–6929.

[66] Qiu, L. B.; He, S. S.; Liu, Z. H.; Ono, L. K.; Son, D. Y.; Liu, Y. Q.; Tong, G. Q.; Qi, Y. B. Rapid hybrid chemical vapor deposition for efficient and hysteresis-free perovskite solar modules with an operation lifetime exceeding 800 hours. *J. Mater. Chem. A* **2020**, *8*, 23404–23412.

[67] Gao, L. L.; Chen, L.; Huang, S. Y.; Li, X. L.; Yang, G. J. Series and parallel module design for large-area perovskite solar cells. *ACS Appl. Energy Mater.* **2019**, *2*, 3851–3859.

[68] Grancini, G.; Roldán-Carmona, C.; Zimmermann, I.; Mosconi, E.; Lee, X.; Martineau, D.; Narbey, S.; Oswald, F.; De Angelis, F.; Graetzel, M. et al. One-year stable perovskite solar cells by 2D/3D interface engineering. *Nat. Commun.* **2017**, *8*, 15684.

[69] Liu, W.; Liu, N. J.; Ji, S. L.; Hua, H. F.; Ma, Y. H.; Hu, R. Y.; Zhang, J.; Chu, L.; Li, X. A.; Huang, W. Perfection of perovskite grain boundary passivation by rhodium incorporation for efficient and stable solar cells. *Nano-Micro Lett.* **2020**, *12*, 119.

[70] Zeng, J.; Bi, L. Y.; Cheng, Y. H.; Xu, B. M.; Jen, A. K. Y. Self-assembled monolayer enabling improved buried interfaces in blade-coated perovskite solar cells for high efficiency and stability. *Nano Res. Energy* **2022**, *1*, e9120004.

[71] Li, X. D.; Zhang, W. X.; Guo, X. M.; Lu, C. Y.; Wei, J. Y.; Fang, J. F. Constructing heterojunctions by surface sulfidation for efficient inverted perovskite solar cells. *Science* **2022**, *375*, 434–437.

[72] Chen, Y. M.; Lei, Y. S.; Li, Y. H.; Yu, Y. G.; Cai, J. Z.; Chiu, M. H.; Rao, R.; Gu, Y.; Wang, C. F.; Choi, W. et al. Strain engineering and epitaxial stabilization of halide perovskites. *Nature* **2020**, *577*, 209–215.

[73] Rolston, N.; Bush, K. A.; Printz, A. D.; Gold-Parker, A.; Ding, Y. C.; Toney, M. F.; McGehee, M. D; Dauskardt, R. H. Engineering stress in perovskite solar cells to improve stability. *Adv. Energy Mater.* **2018**, *8*, 1802139.

[74] Hu, R. Y.; Ge, C. Y.; Chu, L.; Feng, Y. F.; Xiao, S. S.; Ma, Y. H.; Liu, W.; Li, X. A.; Nazeeruddin, M. K. Novel photoelectric material of perovskite-like (CH$_3$)$_3$SPbI$_3$ nanorod arrays with high stability. *J. Energy Chem.* **2021**, *59*, 581–588.

[75] Zhou, T.; Xu, Z. Y.; Wang, R.; Dong, X. Y.; Fu, Q.; Liu, Y. S. Crystal growth regulation of 2D/3D perovskite films for solar cells with both high efficiency and stability. *Adv. Mater.* **2022**, *34*, 2200705.

[76] Qiu, L. B.; Liu, Z. H.; Ono, L. K.; Jiang, Y.; Son, D. Y.; Hawash, Z.; He, S. S.; Qi, Y. B. Scalable fabrication of stable high efficiency perovskite solar cells and modules utilizing room temperature sputtered SnO$_2$ electron transport layer. *Adv. Funct. Mater.* **2019**, *29*, 1806779.

[77] Aitola, K.; Sonai, G. G.; Markkanen, M.; Kaschuk, J. J.; Hou, X. L.; Miettunen, K.; Lund, P. D. Encapsulation of commercial and emerging solar cells with focus on perovskite solar cells. *Sol. Energy* **2022**, *237*, 264–283.

[78] Kosasih, F. U.; Rakocevic, L.; Aernouts, T.; Poortmans, J.; Ducati, C. Electron microscopy characterization of P3 lines and laser scribing-induced perovskite decomposition in perovskite solar modules. *ACS Appl. Mater. Interfaces* **2019**, *11*, 45646–45655.

[79] Carolus, J.; Merckx, T.; Purohit, Z.; Tripathi, B.; Boyen, H. G.; Aernouts, T.; De Ceuninck, W.; Conings, B.; Daenen, M. Potential-induced degradation and recovery of perovskite solar cells. *Sol. RRL* **2019**, *3*, 1900226.

[80] Brecl, K.; Jošt, M.; Bokalič, M.; Ekar, J.; Kovač, J.; Topič, M. Are perovskite solar cell potential-induced degradation proof? *Sol. RRL* **2022**, *6*, 2100815.

[81] Bi, E. B.; Tang, W. T.; Chen, H.; Wang, Y. B.; Barbaud, J.; Wu, T. H.; Kong, W. Y.; Tu, P.; Zhu, H.; Zeng, X. Q. et al. Efficient perovskite solar cell modules with high stability enabled by iodide diffusion barriers. *Joule* **2019**, *3*, 2748–2760.

[82] Yuan, Y. B.; Chae, J.; Shao, Y. C.; Wang, Q.; Xiao, Z. G.; Centrone, A.; Huang, J. S. Photovoltaic switching mechanism in lateral structure hybrid perovskite solar cells. *Adv. Energy Mater.* **2015**, *5*, 1500615.

[83] Bu, T. L.; Shi, S. W.; Li, J.; Liu, Y. F.; Shi, J. L.; Chen, L.; Liu, X. P.; Qiu, J. H.; Ku, Z.; Peng, Y. et al. Low-temperature presynthesized crystalline tin oxide for efficient flexible perovskite solar cells and modules. *ACS Appl. Mater. Interfaces* **2018**, *10*, 14922–14929.

Liang Chu received his Ph.D. degree of condensed matter physics from Huazhong University of Science and Technology in 2014. Now he is a full professor at Hangzhou Dianzi University. His current research interest focuses on perovskite solar cells and optoelectronic memristors.

Jing Zhang received her Ph.D. degree from the Institute of Chemistry, Chinese Academy of Sciences in 2011. After working at the University of Florida in 2011–2012, and National Center for Nanoscience and Technology in 2013–2015 as a postdoctor, she joined Changzhou University in 2016. Her current research area includes perovskite solar cells and organic hole-transport materials.

Wensheng Yan earned his Ph.D. degree of microelectrons from Nanjing University in 2008. Then, he worked overseas from Nanyang Technological University of Singapore to Swinburne University of Science and Technology of Australia, and to Karlsruhe Institute of Technology of Germany. During that time of period of time, he won two prestigious fellowships including Australian Renewable Energy Agency Fellowship in Australia and Experienced Humboldt Fellowship in Germany. He was once a principal investigator of the solar cell project from German Research Foundation. In 2021, Prof. Yan joined Hangzhou Dianzi University of China as a full professor. His research area is mainly photovoltaics including silicon solar cells, perovskite solar cells, and tandem solar cells.